Simulation of electron thermal transport in H-mode discharges

T. Rafiq, A. Y. Pankin, G. Bateman, A. H. Kritz, and F. D. Halpern

Additional information on Phys. Plasmas

Journal Homepage: http://pop.aip.org/
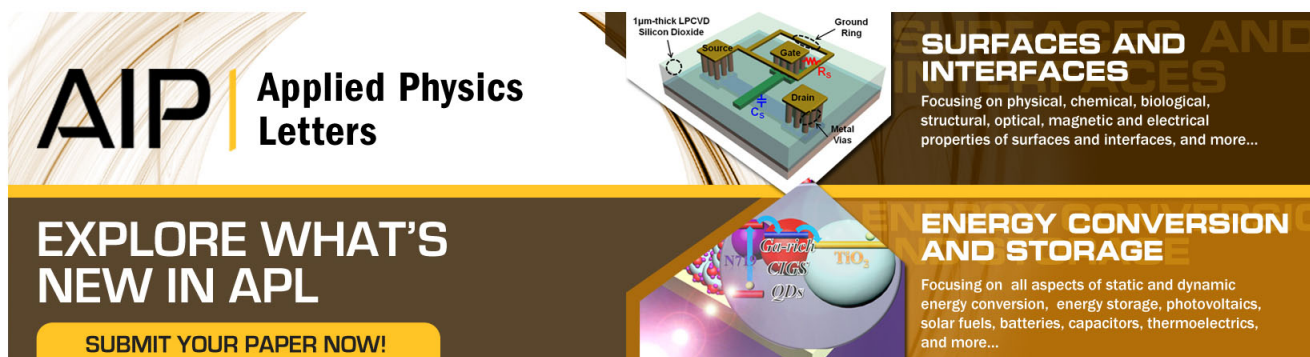
Journal Information: http://pop.aip.org/about/about_the_journal

Top downloads: http://pop.aip.org/features/most_downloaded

Information for Authors: http://pop.aip.org/authors

Simulation of electron thermal transport in *H*-mode discharges

T. Rafiq, A. Y. Pankin, G. Bateman, A. H. Kritz, and F. D. Halpern
Department of Physics, Lehigh University, 16 Memorial Drive East, Bethlehem, Pennsylvania 18015, USA

Electron thermal transport in DIII-D *H*-mode tokamak plasmas [J. L. Luxon, Nucl. Fusion **42**, 614 (2002)] is investigated by comparing predictive simulation results for the evolution of electron temperature profiles with experimental data. The comparison includes the entire profile from the magnetic axis to the bottom of the pedestal. In the simulations, carried out using the automated system for transport analysis (ASTRA) integrated modeling code, different combinations of electron thermal transport models are considered. The combinations include models for electron temperature gradient (ETG) anomalous transport and trapped electron mode (TEM) anomalous transport, as well as a model for paleoclassical transport [J. D. Callen, Nucl. Fusion **45**, 1120 (2005)]. It is found that the electromagnetic limit of the Horton ETG model [W. Horton *et al.*, Phys. Fluids **31**, 2971 (1988)] provides an important contribution near the magnetic axis, which is a region where the ETG mode in the GLF23 model [R. E. Waltz *et al.*, Phys. Plasmas **4**, 2482 (1997)] is below threshold. In simulations of DIII-D discharges, the observed shape of the *H*-mode edge pedestal is produced when transport associated with the TEM component of the GLF23 model is suppressed and transport given by the paleoclassical model is included. In a study involving 15 DIII-D *H*-mode discharges, it is found that with a particular combination of electron thermal transport models, the average rms deviation of the predicted electron temperature profile from the experimental profile is reduced to 9% and the offset to −4%. © *2009 American Institute of Physics*.
[DOI: 10.1063/1.3088027]

I. INTRODUCTION

The objective of this paper is to test models for electron thermal transport and determine a combination of models that yields profiles that are consistent with profiles measured in DIII-D discharges from the magnetic axis to the bottom of the *H*-mode pedestal at the edge of the plasma. Different combinations of electron thermal transport models are tested by carrying out simulations in which the electron temperature profile is predicted while the ion temperature profile is taken from experimental data and the profiles are coupled through equipartition.

The models used to compute electron thermal transport include models for the electron temperature gradient mode (ETG), the trapped electron mode (TEM), and paleoclassical transport. These models provide contributions to transport that are different in the plasma core than at the plasma edge. For example, ETG and TEM modes contribute to transport mostly in the plasma core while the paleoclassical transport contributes significantly at the plasma edge. Two models for ETG anomalous thermal transport are considered: One is the ETG component of the gyro-Landau-fluid (GLF23) transport model;[1] the second is the Horton model for ETG anomalous transport[2] modified with a threshold of Jenko *et al.*[3] Only the long wavelength (electromagnetic) component of the Horton ETG model is included when combined with the GLF23 model since the GLF23 model already includes the ETG transport associated with the short wavelength (electrostatic) turbulence. In one of the thermal transport model combinations that is considered, the TEM is assumed to be suppressed due to flow and magnetic shear. It is anticipated that the ETG mode is likely to be unaffected, or at most, weakly

affected by sheared flows due to its short wavelength nature.

The GLF23 model for electron transport, the Horton ETG model, and the paleoclassical model are implemented in the integrated transport code automated system for transport analysis (ASTRA). Simulations carried out with different combinations of electron transport models are compared to one another and with experimental data for 15 DIII-D *H*-mode discharges[4] spanning a range of plasma parameters. The structure of this paper is as follows: In Sec. II, an overview of the simulation methodology is provided including a description of the GLF23 model; the Horton ETG model in the electromagnetic limit; and the paleoclassical model. Section III contains a description of 15 DIII-D experimental discharges that span a variety of operating conditions. The experimental electron temperature profiles obtained for these discharges are used in the validation of simulation results presented in Sec. IV. Simulations are carried out in which different combinations of the electron thermal transport models are used. The results of these simulations are compared in Sec. IV with the experimental profiles from the 15 DIII-D *H*-mode discharges. The conclusions of the present work are summarized in Sec. V.

II. SIMULATION MODELS

A. GLF23 model

GLF23 (Ref. 1) is a quasilinear gyrofluid transport model that is used to compute the anomalous transport driven by ITG mode, ETG mode, and TEM. The GLF23 model includes kinetic effects through the use of GLF23 equations. It also includes the $\mathbf{E} \times \mathbf{B}$ flow shear and Shafra-

nov shift stabilization. The GLF23 model can be used to compute the anomalous ion and electron thermal transport, particle transport, and momentum transport. The model uses ten wave numbers for the long wavelength ITG/TEM modes and ten wave numbers for the short wavelength ETG modes in the electrostatic limit. The ETG mode is assumed to be a dual of the ITG mode. Because of the strong resemblance between ETG modes and ITG modes, the role of electrons and ions are reversed in the models associated with these two modes. That is, the ions are assumed to be adiabatic in the ETG mode, and the electrons are assumed to be adiabatic in the ITG mode. In general, the electron thermal diffusivity in the GLF23 model (χ_e^{GLF}) can be written as a linear combination of thermal diffusivities driven by ETG modes, $\chi_{\text{ETG}}^{\text{GLF}}$, and TEMs, $\chi_{\text{TEM}}^{\text{GLF}}$, so that

$$\chi_e^{\text{GLF}} = \chi_{\text{ETG}}^{\text{GLF}} + \chi_{\text{TEM}}^{\text{GLF}}. \tag{1}$$

When magnetic shear and flow shear effects stabilize the longer wavelength TEM modes, the shorter wavelength ETG modes usually persist to drive electron thermal transport, in general agreement with experimental observation.

B. Horton ETG model

The Horton (WH) ETG model for electron thermal transport was developed as a generalization of a hydrodynamic theory for short wavelength ETG turbulence with electromagnetic effects included.[5] The model was then calibrated using data from fast wave electron heated Tore Supra discharges with hot electrons.[2] In this model, it is assumed that the ETG mode is a toroidal version of the lower hybrid drift mode driven unstable by charge separation due to the unfavorable ∇B and curvature electron drift in the presence of an electron temperature gradient. The resulting instability can drive short wavelength drift wave turbulence and electron thermal transport in tokamaks.

In the nonlinear regime, it is assumed that the turbulence is driven in two space scale regimes. The short wavelength regime is electrostatic, where the maximum linear growth pumps energy into the electrostatic turbulence, while the long wavelength regime is neutrally stable. The ETG fluctuation spectrum mode couples energy to longer space scale fluctuations. This inverse cascade, or mode coupling of shorter space scale electrostatic fluctuations to longer space scales, drives a coupling to the parallel vector potential $A_\parallel$ fluctuations at the scale of electromagnetic skin depth c/ω_{pe}. At this scale, the fluctuations become neutrally stable electromagnetic vortices.

This secondary driven electromagnetic turbulence is expected to lead to a large stochastic diffusion of the trapped electrons.[6] Stochastic transport studies indicate that, once the turbulence level reaches the mixing length level, the electron diffusivity is insensitive to the details of the fluctuation spectrum and, under these conditions, the electron diffusivity is governed by a random walk of the trapped electrons over the skin depth correlation length, c/ω_{pe}, at the rate of the decorrelation frequency, which is of the order of bounce frequency of the trapped electrons. For the long wavelength part of the spectrum, stochasticity occurs due to the overlap of the vortex circulation frequency with the parallel bounce frequency, which produces a strong diffusion of the trapped electrons and a weak diffusion of the passing electrons.

As noted above, to avoid double counting of the contribution of short wave turbulence when the Horton (WH) ETG model is combined with the GLF23 ETG model, only the electromagnetic contribution to the Horton model for electron thermal conductivity is considered. In the WH ETG model,[2] the electron thermal diffusivity in the electromagnetic limit (χ_{EM}) can be written

$$\chi_{\text{EM}} = C_e^{\text{em}} \left(\frac{c^2}{\omega_{\text{pe}}^2} \right) \left(\frac{v_{\text{The}}}{\sqrt{L_{\text{Te}}R}} \right), \quad l_{c,e}^{\text{es}} < \delta_e, \tag{2}$$

where $C_e^{\text{em}} = 0.082$, c is the speed of light, ω_{pe} is the plasma frequency, $v_{\text{The}} = \sqrt{T_e/m_e}$, is the electron thermal velocity (T_e is the electron temperature and m_e is the mass of electron), R is the major radius, $L_{\text{Te}} = (d \ln T_e/d\rho)^{-1}$ is the electron temperature gradient scale length, $l_{c,e}^{\text{es}} \equiv q\rho_e R/L_{\text{Te}}$ is the electron mixing length, and $\delta_e \equiv c/\omega_{\text{pe}}$ is the collisionless skin depth (ρ_e is the electron gyroradius and e is the electron charge). Under typical experimental conditions, $l_{c,e}^{\text{es}} < \delta_e$ for $r/a \leq 0.3$, where r is the minor radius of a magnetic surface and a is the minor radius at the edge of the plasma.

The Horton ETG model diffusivity is refined by using the Jenko model for the threshold of the electrostatic ETG mode[3]

$$\chi_{\text{EM}}^{\text{WH}}$$
$$= \begin{cases} 0, & R/L_{\text{Te}} < (R/L_{\text{Te}})^{\text{cr}}, \\ \chi_{\text{EM}} \tanh((R/L_{\text{Te}} - (R/L_{\text{Te}})^{\text{cr}})), & R/L_{\text{Te}} > (R/L_{\text{Te}})^{\text{cr}}, \end{cases} \tag{3}$$

where χ_{EM} is given in Eq. (2). Here, $(R/L_{\text{Te}})^{\text{cr}}$ is the normalized critical toroidal electron temperature gradient which is derived from comprehensive linear toroidal gyrokinetic simulations[3] to be

$$(R/L_{\text{Te}})^{\text{cr}} = \max\left[\left(1 + \frac{Z_{\text{eff}}T_e}{T_i} \right) \left(1.33 + \frac{1.91s}{q} \right)(1 - 1.5\varepsilon) \right.$$
$$\left. \times \left(1 + 0.3\varepsilon\frac{d\kappa}{d\varepsilon} \right), 0.8\frac{R}{L_n} \right], \tag{4}$$

where q is the magnetic safety factor, $\varepsilon = r/R$ is the inverse aspect ratio, and κ is the elongation of the magnetic surface.

C. Paleoclassical model

It has been hypothesized[7] that part of the radial electron heat transport in current-carrying, magnetically confined, toroidal plasmas results from paleoclassical Coulomb collision processes. These processes involve parallel electron heat conduction and magnetic field diffusion. In this model, the electron temperature equilibrates along magnetic field lines while diffusing field lines carry this equilibrated electron temperature with them, which results in a radial electron heat diffusivity given by[8]

TABLE I. Plasma parameters for DIII-D power, n_e, ρ_*, and β scans. Values of the simulated electron pedestal temperatures obtained with the model that provides the best overall fit to the electron temperature profiles are included.

Tokamak	DIII-D	DIII-D	DIII-D	DIII-D	DIII-D	DIII-D	DIII-D	DIII-D	DIII-D
Discharge	77557	77559	81321	81329	82205	82788	90117	90108	99411
Type	Low power	High power	Low n_e	High n_e	Low ρ_*	High ρ_*	Low β	High β	High performance
R (m)	1.68	1.69	1.69	1.70	1.68	1.68	1.67	1.68	1.66
a (m)	0.60	0.61	0.56	0.58	0.60	0.59	0.58	0.59	0.54
κ	1.85	1.84	1.83	1.83	1.71	1.67	1.80	1.81	1.84
δ	0.33	0.35	0.29	0.36	0.37	0.35	0.27	0.25	0.56
B_T (T)	2.00	2.00	1.98	1.97	1.81	0.95	1.60	1.91	1.63
I_p (MA)	1.00	1.00	0.99	1.00	1.34	0.66	1.13	1.35	1.20
$\bar{n}_{e,19}$	4.88	5.02	2.94	5.35	5.34	2.86	3.15	6.96	4.72
Z_{eff}	1.68	2.21	2.42	1.65	2.13	1.94	2.38	1.83	2.40
P_{NB} (MW)	4.73	13.23	3.49	8.34	5.86	3.25	1.15	5.84	9.16
$n_{e,19,ped}^{exp}$	3.22	3.38	2.13	3.38	3.93	2.28	2.32	6.72	3.47
$T_{i,ped}^{exp}$ (keV)	0.44	0.27	1.32	0.55	0.95	0.57	0.38	0.50	1.69
$T_{e,ped}^{exp}$ (keV)	0.50	1.02	0.70	0.54	0.80	0.47	0.20	0.37	0.82
$T_{e,ped}^{sim}$ (keV)	0.48	0.63	0.56	0.42	0.70	0.42	0.24	0.34	1.00
t_{diag} (s)	2.70	2.70	3.90	3.80	3.66	3.54	2.96	3.09	1.80

$$\chi_e^{paleo} = \frac{3}{2}(M+1)D_\eta, \quad M \simeq \frac{1}{\pi R q} \frac{1}{1/\lambda_e + 1/l_{max}},$$

$$D_\eta \equiv \frac{\eta_\parallel^{nc}}{\mu_0}, \tag{5}$$

where M is the helical multiplier caused by helically resonant radial diffusion[8] in the vicinity of the medium order rational surfaces; R is the average major radius, q is the safety factor; λ_e is the electron collision length which can be written as

$$\lambda_e \equiv v_{Te}/\nu_e \simeq 1.2 \times 10^{16} \frac{T_e}{Z_{eff} n_e} \left(\frac{17}{\ln \Lambda} \right), \tag{6}$$

where $\ln \Lambda$ is the Coulomb logarithm, $Z_{eff} \equiv \Sigma n_i Z_i^2 / n_e$ is the effective ion charge, n_e is the electron density, T_e is the electron temperature in eV, $l_{max} = \pi R q n_{max}$ is the length over which magnetic field lines diffuse radially, and $n_{max} = (\pi \bar{\delta}_e |q'|)^{-1/2}$. In this notation, the primed quantity indicates a derivative with respect to the normalize radial coordinate ρ; $\bar{\delta}_e = c/\omega_{pe}a$ is the normalized electromagnetic skin depth; ω_{pe} is the plasma frequency and a is the plasma minor radius. D_η is the magnetic field diffusivity and is the fundamental parameter of the paleoclassical transport model; $\eta_\parallel^{nc}$ is the parallel neoclassical resistivity, which is evaluated in this paper using the NCLASS code;[9] and $\mu_0 \equiv 4\pi \times 10^{-7}$.

The conditions limiting the regimes of the paleoclassical electron heat diffusivity are as follows. For collisionless region ($\lambda_e > l_{max}$):

$$\chi_{eI}^{paleo} = \frac{3}{2} \frac{\eta_\parallel^{nc}}{\mu_0} n_{max}, \tag{7}$$

for collisional region ($l_{max} > \lambda_e > \pi R q$):

$$\chi_{eII}^{paleo} = \frac{3}{2} \frac{v_{Te}}{\pi R q} \frac{c^2}{\omega_{pe}^2} \frac{\eta_\parallel^{nc}}{\eta_0}, \tag{8}$$

and for edge region ($\pi R q > \lambda_e > \pi R$):

$$\chi_{eIII}^{paleo} = \frac{10^3 Z_{eff}}{T_e(eV)^{3/2}}, \tag{9}$$

where $\eta_0 \equiv m_e \nu_e / n_e e^2$ is the perpendicular electrical resistivity, m_e is the electron mass, e is the electron charge, and ν_e is the electron collision frequency.

III. DIII-D H-MODE DATA

Experimental data from 15 DIII-D H-mode discharges spanning a variety of operating conditions are considered in this paper. Data are taken from the International Profile Database,[10] except for discharges 98889 and 97887, which were recently reanalyzed.[11] Data were processed by either the TRANSP code (http://w3.pppl.gov.transp) or the ONETWO code (http://fusion.gat.com/onetwo/), which are time-dependent transport analysis codes. Some of the relevant experimental parameters for the 15 DIII-D H-mode discharges are listed in Tables I and II, including: The major radius, R (m); the minor radius, a (m); the elongation, κ; the triangularity, δ; the vacuum toroidal magnetic field, B_T (T), at major radius R; the toroidal plasma current, I_p (MA); the line-averaged electron density, $\bar{n}_{e,19}$, in units of 10^{19} m^{-3}; the average Z_{eff}; the neutral beam injection power passing through the wall of the tokamak, P_{NB} (MW), which is not necessarily the absorbed power; the electron density $n_{e,19,ped}^{exp}$, electron temperature $T_{e,ped}^{exp}$ (keV), and the ion temperature $T_{i,ped}^{exp}$ (keV) from experimental data at approximately the top of the pedestal as well as the corresponding electron temperature at the top of the pedestal, $T_{e,ped}^{sim}$ (keV), from simulations described below. The last item in each table is the diagnostic time, t_{diag} (s), during each discharge at which the

TABLE II. Plasma parameters for the DIII-D elongation and triangularity scan discharges. Values of the simulated electron pedestal temperatures obtained with the model that provides the best overall fit to the electron temperature profiles are included.

Tokamak	DIII-D	DIII-D	DIII-D	DIII-D	DIII-D	DIII-D
Discharge	81499	81507	82188	82183	98889	97887
Type	Low κ	High κ	Low κ	High κ	Low δ	High δ
R (m)	1.69	1.61	1.69	1.60	1.6955	1.68
a (m)	0.61	0.52	0.61	0.52	0.77	0.61
κ	1.68	1.95	1.65	1.91	1.78	1.82
δ	0.32	0.29	0.29	0.22	0.03	0.85
B_T (T)	1.91	1.91	1.57	1.63	2.005	2.1
I_p (MA)	1.35	1.34	1.33	1.33	1.21	1.55
$\bar{n}_{e,19}$	4.81	4.90	6.47	6.87	4.0	4.6
Z_{eff}	2.33	1.93	1.83	1.95	2.5	2.35
P_{NB} (MW)	5.74	5.71	3.86	3.85	3.14	7.10
$n_{e,19,\text{ped}}^{\text{exp}}$	4.01	3.24	4.97	4.97	2.85	4.73
$T_{i,\text{ped}}^{\text{exp}}$ (keV)	0.83	1.18	0.48	0.51	0.88	1.00
$T_{e,\text{ped}}^{\text{exp}}$ (keV)	0.74	1.17	0.25	0.47	0.68	1.4
$T_{e,\text{ped}}^{\text{sim}}$ (keV)	0.46	0.63	0.29	0.35	0.53	1.18
t_{diag} (s)	4.00	3.8	3.775	3.775	2.23	2.23

simulation profiles, described in Sec. IV are compared with the experimentally measured profiles.

The values of simulated electron pedestal temperature, $T_{e,\text{ped}}^{\text{sim}}$ (keV), that are given in Tables I and II are obtained using the model given in Eq. (11) described in Sec. IV below, using software that fits a modified tangent hyperbolic (mtanh) function to experimental and simulated pedestal profiles in the DIII-D tokamak.[12] The modified tanh (mtanh) function provides analytic fits to DIII-D pedestal density, temperature and pressure profiles that are used to compute estimates of the gradients, heights and other characteristics of these profiles. The MTANH fitting code is adaptive in that it uses the input data to make an initial estimate of the fit parameters and then refines the estimate. A key feature of this initialization process is that the code searches for the region of steepest gradient in the data and then the location of the symmetry point in the fit function is set in that region. In addition, the algorithm is used to compute bounds on the fit parameters during the fitting procedure. These bounds are also determined adaptively during the initialization of the fit parameters.

The wide variety of 15 DIII-D *H*-mode discharges include a ρ_* scan, a β scan, a density scan, a power scan, two pairs of elongation (κ) scans, and a high performance discharge. The plasma parameters listed in Tables I and II indicate that the elongation at the plasma edge spans the range of $1.65 \leq \kappa \leq 1.95$, the edge triangularity spans the range of $0.03 \leq \delta \leq 0.85$, the magnetic field strength spans the range of $0.95 \leq B \leq 2.1$ T, the plasma current spans the range of $0.66 \leq I_p \leq 1.55$ MA, the line-averaged density spans the range of $2.86 \leq \bar{n}_{e,19} \leq 6.96$, and the beam power spans the range $3.14 \leq P_{\text{NB}} \leq 13.23$ MW.

Discharges 77557 and 77559 represent a power scan in which the heating power was varied while the average plasma density was held constant.[13] A power balance analysis of these discharges indicates that both the electron and ion diffusivities increase with increasing temperature. Discharges 81321 and 81329 represent a density scan at constant temperature. A power balance analysis of these discharges indicates that the electron and ion diffusivities are both independent of the density.[10,13] Discharges 82205 and 82788 are part of a DIII-D ρ_* scan designed to have the same plasma shape as well as the same beta, collisionality, and safety factor as ITER. An analysis of the heat transport in these discharges found that the electron and ion diffusivities and that the thermal confinement time all follow approximately gyro-Bohm scaling.[14] The two pairs of elongation scans, discharges 81499–81507 and 82183–82188, were conducted to test predictions of discharges with improved fusion performance at higher elongation. In these scans, it is observed[15] that the plasma temperature increases with elongation while other parameters (density, safety factor, heating power) are held fixed. In the β scan, which is represented by discharges 90117 and 90108, β was varied while the ρ_*, ν_*, and q, were all kept constant. A slightly favorable beta scaling of the confinement time was found in this scan.[16] Discharge 97887 is a high triangularity ($\delta = 0.85$), high performance discharge, with a long ELM-free period early in the discharge (an ELM occurs shortly after 2.23 s); the pedestal parameters are shown for a time just prior to the first ELM, which has been analyzed in detail.[17] Discharge 98889 has the lowest triangularity plasma shape ($\delta = 0.03$) among the discharges considered in this paper.

IV. COMPARISON OF SIMULATED AND EXPERIMENTAL DIII-D *H*-MODE

Electron temperature profiles

The models for electron thermal transport, described in Sec. II, were implemented in the ASTRA integrated modeling code, version 6.1. The ASTRA code, a one and half-dimensional code, includes realistic tokamak geometry and solves coupled equations for the magnetohydrodynamic equilibrium, current diffusion, and heat transport self-consistently. For the simulations presented in this paper, an integrated modeling protocol was established to simulate the electron temperature profile and to compare that profile with DIII-D electron temperature data for 15 *H*-mode discharges. The simulations yield the electron temperature profile from the magnetic axis to the base of the *H*-mode pedestal at the plasma edge, not including the separatrix or the scrape-off layer. In simulating the electron temperature profile, other profiles such as the electron and ion density, the ion temperature, the effective ion charge (Z_{eff}), and the magnetic q profile are taken from experimental data. The equilibrium boundary shape, as a function of time, is also taken from the experimental data.

The ASTRA code, although time dependent, was used in this paper to compute nearly steady state profiles. In discharges with broad sawtooth crashes, the temperature profiles usually achieve nearly steady state conditions before the subsequent sawtooth crash. After a transient period that follows the crash, the temperatures return to nearly steady state conditions. The comparisons of simulation results with experimental data were made at times when the saturated nearly steady state conditions apply. Since the q-profile in these simulations is obtained from analysis of experimental data, the q-profile has the appropriate form for the saturated conditions that exist prior to each sawtooth crash. Consequently, for a discharge with broad sawtooth crashes, the central part of the ASTRA simulated temperature profiles will not differ significantly from the profiles obtained just prior to a sawtooth crash in fully time-dependent simulations. In a discharge with narrower sawtooth oscillations, with a mixing radius that is of the order of only 10% of the plasma radius minor radius, the sawtooth oscillations are less likely to saturate in the way that they do in discharges with broad sawtooth oscillations. However, the region affected by narrow sawtooth oscillations is correspondingly small and, consequently, they have less of an effect on the overall shape of the temperature profiles.

Transport models consisting of different combinations of components were used to compute the electron thermal transport through the plasma. The resulting electron temperature profiles, obtained from simulations using different combinations of transport models, were compared to experimental electron temperature data for the fifteen DIII-D discharges considered. Simulations were carried out using the five different combinations of models for χ_e, shown below, in a search for the electron thermal transport model that yields the best agreement between simulation results and experimental data:
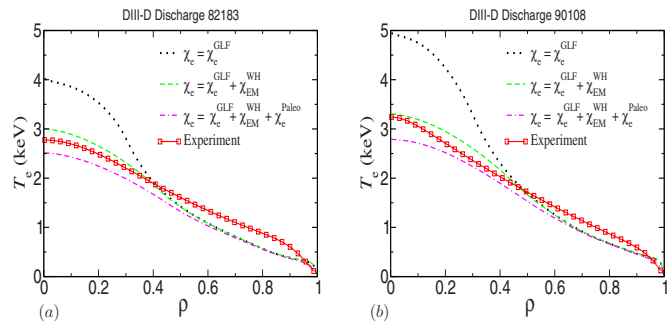

FIG. 1. (Color online) The experimental and simulated electron temperature profiles for DIII-D discharge 82183 (left panel) and 90108 (right panel). Different curves represent simulations carried out using different electron thermal transport models.

$$\chi_e = \begin{cases} \chi_e^{GLF}, & \text{model 1,} \\ \chi_e^{GLF} + \chi_{EM}^{WH}, & \text{model 2,} \\ \chi_e^{GLF} + \chi_{EM}^{WH} + \chi_e^{paleo}, & \text{model 3,} \\ \chi_{psTEM}^{GLF} + \chi_{EM}^{WH} + \chi_e^{paleo}, & \text{model 4,} \\ \chi_{ETG}^{GLF} + \chi_{EM}^{WH} + \chi_e^{paleo}, & \text{model 5.} \end{cases} \quad (10)$$

Here, χ_{psTEM} in model 4 is χ_e^{GLF} with flow shear adjusted so that TEM (trapped electron mode) contribution to χ_e^{GLF} is stabilized in the pedestal region. In model 5, χ_{ETG}^{GLF} is χ_e^{GLF} with only the ETG (electron temperature gradient) mode contributing to transport.

Neoclassical electron transport is not included models 1–5 since the neoclassical electron transport is negligible and does not affect the simulated electron temperature profiles.

A result of testing different combinations of electron thermal transport models is illustrated in Figs. 1 and 2, in which simulated electron temperature profiles are presented along with experimental data for two DIII-D *H*-mode discharges, 82183 in panel (a) and 90108 in panel (b). It can be seen in panels (a) and (b) of Fig. 1 that simulations using model 1 for electron thermal transport, the GLF23 model by itself, results in overpredicting T_e in the plasma center and underpredicting T_e at the plasma edge (the dotted curves). This trend is generally found in the simulations of the 15 DIII-D *H*-mode discharges.

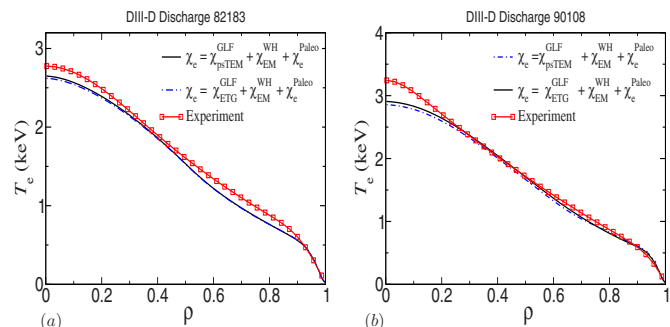The agreement between simulation and experiment is somewhat improved when the electromagnetic component of

FIG. 2. (Color online) The experimental and simulated electron temperature profiles assuming that the TEM is shear stabilized for discharges 82183 and 90108.

the Horton ETG model is added to the GLF23 model (that is model 2, $\chi_e = \chi_e^{\mathrm{GLF}} + \chi_{\mathrm{EM}}^{\mathrm{WH}}$). The simulation results obtained using model 2 are indicated with dashed curves in Fig. 1. With model 2 there is better agreement in the central region of the plasma, but the addition of the Horton ETG model has little effect in the outer edge region of the plasma.

When paleoclassical thermal transport is added to the transport model (simulations with model 3, $\chi_e = \chi_e^{\mathrm{GLF}} + \chi_{\mathrm{EM}}^{\mathrm{WH}} + \chi_e^{\mathrm{paleo}}$), the effect on the electron temperature profile is illustrated with the dotted-dashed curves in Fig. 1, panels (a) and (b). In this combination of models, the inclusion of χ_e^{paleo} does not appear to improve the agreement between simulation and data, particularly at the plasma edge. A shortcoming of the models, used to produce the simulations shown in Fig. 1, is that they do not properly reproduce the *H*-mode pedestal in the electron temperature profile. It will be shown below in this section that when a transport model is used that does produce the *H*-mode pedestal, for example model 5, and the contribution from χ_e^{paleo} is omitted, there in significant degradation of agreement between the simulations and the data.

For model 4, $\chi_e = \chi_{\mathrm{psTEM}}^{\mathrm{GLF}} + \chi_{\mathrm{EM}}^{\mathrm{WH}} + \chi_e^{\mathrm{paleo}}$, it is assumed that the contribution from TEM mode in the GLF23 model is flow shear stabilized in the pedestal region. Temperature profiles that result from using model 4 are shown by the dotted-dashed curves in panels (a) and (b) of Fig. 2. It is seen that the simulated electron temperature pedestal heights are similar to the experimentally observed heights and, in particular a better fit to the profile is obtained in the region of the *H*-mode pedestal. Results for the comparison of profiles obtained with model 4 and the experimental data, shown in Fig. 2, are comparable to corresponding results obtained from simulations of the remaining 14 DIII-D discharges.

It is found, in the study presented in this paper, that the electron thermal diffusivity model combination that yields the best agreement between simulation and experimental data is model 5,

$$\chi_e = \chi_{\mathrm{ETG}}^{\mathrm{GLF}} + \chi_{\mathrm{EM}}^{\mathrm{WH}} + \chi_e^{\mathrm{paleo}}, \quad \text{model 5.} \tag{11}$$

In this model for χ_e, the trapped electron contribution is totally omitted from the GLF23 model. The results obtained using model 5 are illustrated by solid curves in Fig. 2.

The comparisons of the simulated electron temperature profiles, T_e^{sim}, with the experimentally measured electron temperature profiles, T_e^{exp}, are quantified by computing the root-mean-square (rms) deviation and the relative offsets (Offset) between the simulated temperature profile and the experimental data. The rms deviation is computed as

$$\mathrm{rms} = \frac{\sqrt{\Sigma_{j=1}^{N}(T_{ej}^{\mathrm{exp}} - T_{ej}^{\mathrm{sim}})^2}}{\sqrt{\Sigma_{j=1}^{N}(T_{ej}^{\mathrm{exp}})^2}}, \tag{12}$$

where T_{ej}^{exp} is the *j*th experimental electron temperature data point, T_{ej}^{sim} is the corresponding simulated result, and N is the number of experimental data points in the profile. The profile offset is defined as

TABLE III. The averaged rms deviation and the relative offsets in percent between simulated and experimentally measured T_e profiles for fifteen DIII-D *H*-mode discharges.

Electron thermal transport	Model	Average rms (%)	Average offset (%)
$\chi_e = \chi_e^{\mathrm{GLF}}$	1	32	−3
$\chi_e = \chi_e^{\mathrm{GLF}} + \chi_{\mathrm{EM}}^{\mathrm{WH}}$	2	20	−15
$\chi_e = \chi_e^{\mathrm{GLF}} + \chi_{\mathrm{EM}}^{\mathrm{WH}} + \chi_e^{\mathrm{Paleo}}$	3	19	−17
$\chi_e = \chi_{\mathrm{psTEM}}^{\mathrm{GLF}} + \chi_{\mathrm{EM}}^{\mathrm{WH}} + \chi_e^{\mathrm{Paleo}}$	4	14	−11
$\chi_e = \chi_{\mathrm{ETG}}^{\mathrm{GLF}} + \chi_{\mathrm{EM}}^{\mathrm{WH}} + \chi_e^{\mathrm{Paleo}}$	5	9	−4

$$\mathrm{Offset} = \frac{\Sigma_{j=1}^{N} T_{ej}^{\mathrm{sim}} - T_{ej}^{\mathrm{exp}}}{\sqrt{\Sigma_{j=1}^{N}(T_{ej}^{\mathrm{exp}})^2}}. \tag{13}$$

The offset is a measure of the overall underprediction (offset < 0) or overprediction (offset > 0) of the simulated profile relative to experimental data. Note that the rms and Offset definitions used in this paper are those that appear in Ref. 18 and differ from the definitions used in Refs. 19 and 20.

The values of the rms deviations and offsets, averaged over all 15 DIII-D *H*-mode discharges, are shown in Table III for simulations using the five different transport models listed in Eq. (10). When the GLF23 model for electron thermal transport ($\chi_e = \chi_e^{\mathrm{GLF}}$, model 1) is used in the simulation of the electron temperature profiles for all 15 discharges, the average rms deviation is found to be 32% and the average offset is −3%. The average rms deviation is large in this case because the shapes of the simulated profiles are quite different from those of the measured profiles, as illustrated by the dotted lines in Fig. 1. When $\chi_{\mathrm{EM}}^{\mathrm{WH}}$ is included with χ_e^{GLF} (model 2), there is reduction in the average rms to 20% and an increase in the average offset to −15% (i.e., the simulated profiles are lower, on the average, than the experimental data). When χ_e^{paleo} is included in the simulations (model 3), the rms deviation is reduced to 19% and the offset increases to −17%. When the assumption is made that the TEMs are shear stabilized in the pedestal region, i.e., when model 4 is used for χ_e, the average rms deviation decreases to 14% and the offset changes to −11%. Finally, when the contribution from the TEM mode is totally omitted from the electron thermal conductivity, that is for model 5 given in Eq. (11), $\chi_e = \chi_{\mathrm{ETG}}^{\mathrm{GLF}} + \chi_{\mathrm{EM}}^{\mathrm{WH}} + \chi_e^{\mathrm{paleo}}$, the electron temperature profiles have an average rms deviation of 9% and an offset of −4%.

The rms deviations and offsets vary from discharge to discharge. When model 5 [Eq. (11)] is used in the simulations, the resulting rms deviations and offsets for the fifteen DIII-D discharges are shown in the bar graphs that appear Figs. 3 and 4. The rms deviations shown in Fig. 3 vary from a minimum of about 2% to a maximum of about 18%. The offsets shown in Fig. 4 range from about +11% to −17%.

Two discharges are found to have rms deviations larger than 15%: Discharge 77559 is a high power DIII-D discharge and discharge 90117 is the low β DIII-D *H*-mode discharge. Simulation results for the T_e profiles are shown in Fig. 5 for these two discharges, 77559 and 90117, for which the rms deviations are larger 18%. In the case of discharge 90117,
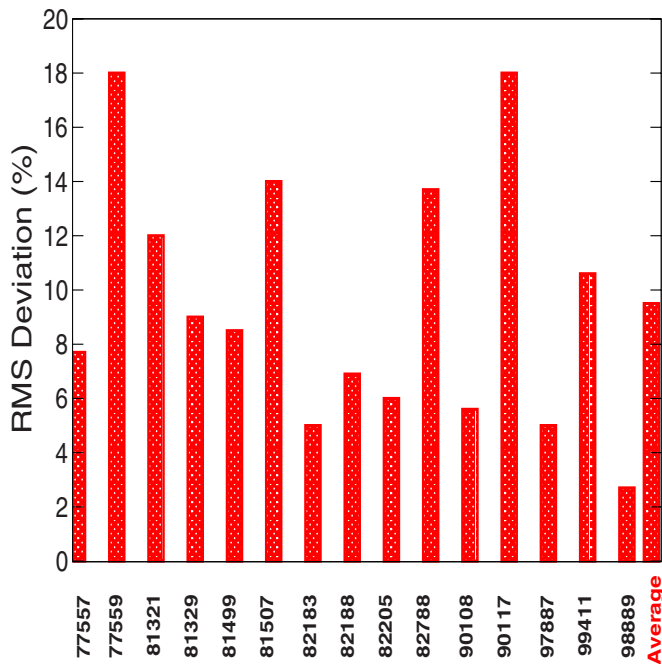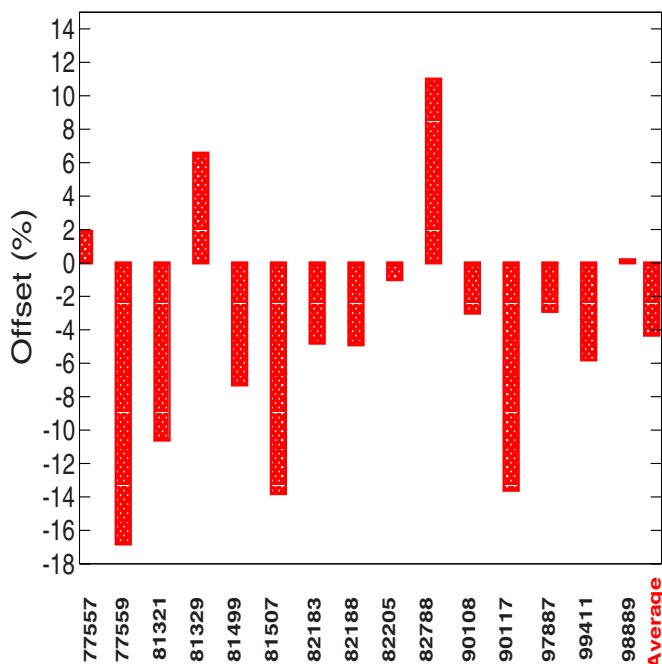
FIG. 3. (Color online) The rms deviations obtained from simulations using model 5 compared to experimental data for fifteen DIII-D *H*-mode discharges.

FIG. 5. (Color online) Simulated and experimental T_e profiles for DIII-D discharges 90117 and 77559. The rms deviations for these two discharges, 18%, are larger than the rms deviations from simulations of the remaining thirteen DIII-D discharges carried out using the model 5.

$< \rho < 0.9$) is too small. For both discharges there is a significant negative offset resulting from the underprediction of the profiles.

The 9% average rms deviation obtained using model 5 for the electron thermal transport may be reduced slightly by calibrating the semiempirical parameter C_e^{em} in the expression for χ_{EM} given in Eq. (2). The value $C_e^{em}=0.082$ is used in the simulation results summarized in Figs. 3 and 4 because that value was the result of a previous calibration using fast wave electron heated Tore Supra discharges with hot electrons described in Ref. 2. Below, the dependence of the simulated electron temperature profile on the choice of the value of C_e^{em} is examined.

The results of varying the semiempirical parameter C_e^{em}, which appears in Eq. (2), are illustrated in Fig. 6 for DIII-D discharge 81499. As the coefficient C_e^{em} is decreased from 0.082 to 0.0605, the rms deviation decreases from 8.5% to 6.9% and the offset changes from -7.3 to -4.8%. A further decrease in the coefficient C_e^{em} to 0.041% changes the rms deviation to 7.3% and the offset to -2.3%. As shown in Fig. 6, the decrease in the C_e^{em} coefficient affects the simulated electron temperature profile in the core region, while the edge region is found to be relatively unaffected. As can be seen in Fig. 4, most of the simulated discharges have negative offsets, indicating underprediction of the T_e profiles. Al-

shown in Fig. 5(a), the whole edge region, including the pedestal, is simulated reasonably accurately. Therefore, the relatively large rms deviation for 90117 is mostly a result of the core transport model used in this simulation, particularly the ETG electromagnetic contribution from the Horton model (χ_{EM}^{WH}). In the case of discharge 77559, shown in Fig. 5(b), the slope of the pedestal is approximately correct but the transport through the edge region near the pedestal (0.8

FIG. 4. (Color online) Offsets obtained from simulations using model 5 compared to experimental data for fifteen DIII-D *H*-mode discharges.
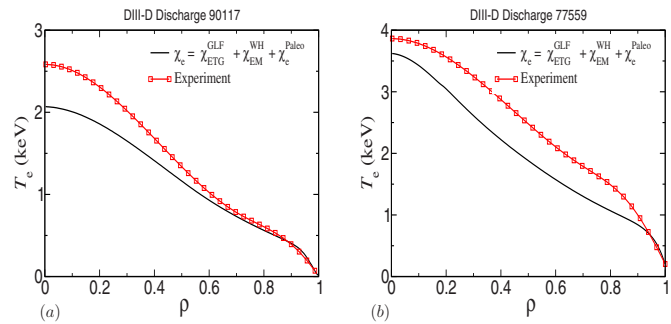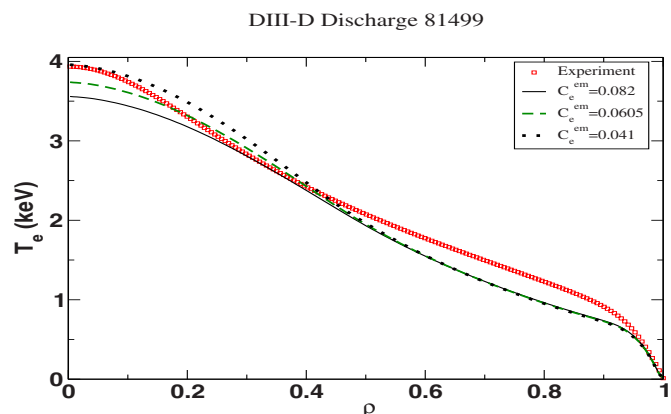

FIG. 6. (Color online) Electron temperature profiles obtained from simulations of discharge 81499 using different values for the coefficient C_e^{em} in Eq. (2) for the electromagnetic ETG electron thermal transport.
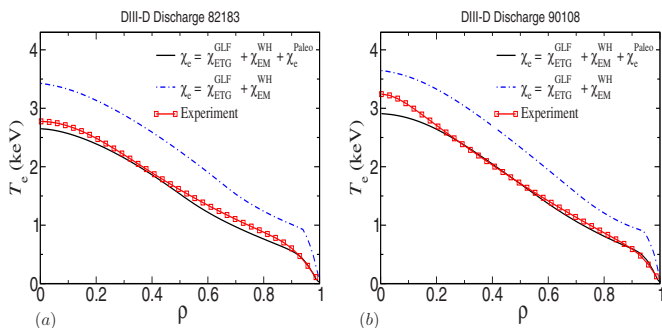
FIG. 7. (Color online) Experimental and simulated T_e profiles with the paleoclassical model included (solid curve) and excluded (dotted-dashed curve) in model 5 for discharges 82183 and 90108.

FIG. 9. (Color online) Total electron thermal diffusivity profile and its components computed using model 5 for DIII-D discharge 82183 (left panel) and 90108 (right panel).

though the magnitudes of these negative offsets are already small, their magnitudes might be further decreased by a new calibration the semiempirical parameter C_e^{em}. However, the result for the average rms deviation is not particularly sensitive to the choice made for the semiempirical parameter C_e^{em}.

The dashed-dotted lines in Fig. 7, panels (a) and (b), indicate the electron temperature profiles, T_e^{sim}, that result from simulations of DIII-D discharges 82183 and 90108 when the paleoclassical model is not included in model 5. The omission paleoclassical model as a component of the transport model results in a significant overprediction of the electron temperature. It is found that inclusion of both the paleoclassical model and the ETG component of the GLF23 model are needed to produce a simulated T_e^{sim} profile that is consistent with the experimental profile in the edge pedestal region ($\rho > 0.9$). In summary, the combination of the electrostatic part of the GLF23 model, χ_{ETG}^{GLF}, combined with the electromagnetic part of the Horton model, χ_{EM}^{WH} and the paleoclassical electron thermal diffusivity, χ_e^{paleo}, produces the closest agreement between the simulated and the experimental T_e profiles. This agreement is illustrated in Fig. 7 for the DIII-D discharges 82183 and 90108.

In Fig. 8(a), the components of the electron thermal diffusivity, χ_e, that contribute to model 5 are shown as a function of normalized minor radius, ρ, for DIII-D discharge 98889. The corresponding electron temperature profile is shown in Fig. 8(b). The components of χ_e for model 5 are shown for DIII-D discharges 82183 and 90108 in the left and right panels of Fig. 9 while the corresponding electron tem-
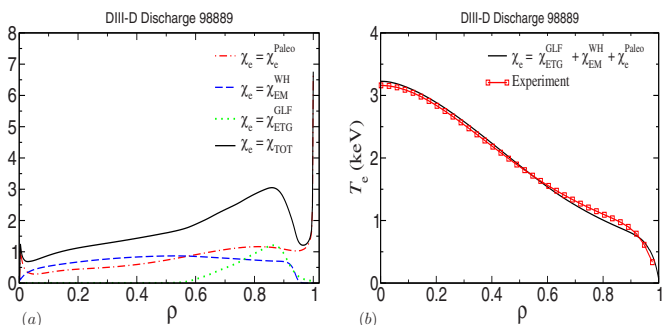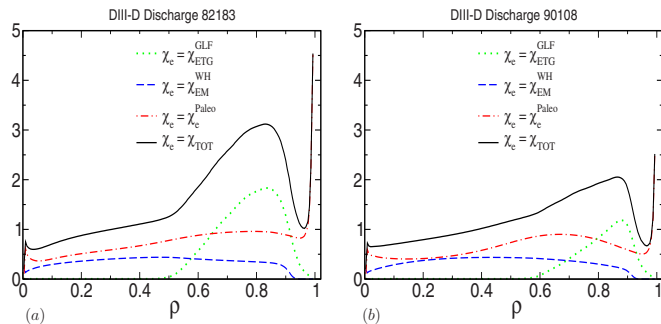

FIG. 8. (Color online) (a) Total electron thermal diffusivity profile and its components computed using model 5 (left panel) and (b) simulated and experimental T_e profiles (right panel) for DIII-D 98889 discharge.

perature profiles for those discharges are shown in the left and right panels of Fig. 2. In Figs. 8 and 9 it can be seen that the electromagnetic contribution to electron thermal transport driven by ETG modes, χ_{EM}^{WH}, is significant in the deep core region (roughly, the inner half of the plasma). The electrostatic contribution driven by ETG modes, χ_{ETG}^{GLF} dominates in the outer part of the plasma up to the top of the pedestal. The contribution of the paleoclassical model is dominant in the pedestal region, but also contributes significantly in the plasma core.

An accurate simulation of the pedestal region is important because the height of the pedestal strongly influences the confinement of the core plasma.[21,22] It has been found in simulations of *H*-mode plasmas that the height of the pedestal has a large effect on the shape of the temperature and density profiles and, consequently, a large effect on the global confinement scaling.[20,23] The simulated pedestal height of the electron temperature, T_{ped}^{sim} (keV), computed using model 5 given in Eq. (11), and the corresponding experimental electron temperature pedestal height T_{ped}^{exp} (keV), are shown in Tables I and II. When statistics for the height of the electron temperature pedestal are averaged over all fifteen discharges, the rms deviation is approximately 29% and the corresponding offset is approximately −17%. If two discharges were excluded—the high power discharge, 77559, and the high elongation discharge, 81507—the average rms deviation for the pedestal height would be reduced to about 20% and the average pedestal offset would be −11%.

Note that only the electron temperature profile is computed in the simulations presented in this paper. The ion temperature and other profiles are taken from experimental data. If both the electron and ion temperature profiles were predicted from the transport model corresponding to model 5, the change in the electron temperature profile is found to be small. This small change is illustrated in Fig. 10, where the solid line shows the electron temperature profile that is simulated using experimental data for the ion temperature profile while the dashed-dotted line shows the electron temperature profile that is simulated together with the ion temperature profile using model 5.

V. SUMMARY

The electron thermal transport from the magnetic axis to the bottom of the pedestal is investigated with predictive integrated modeling simulations using combinations of three
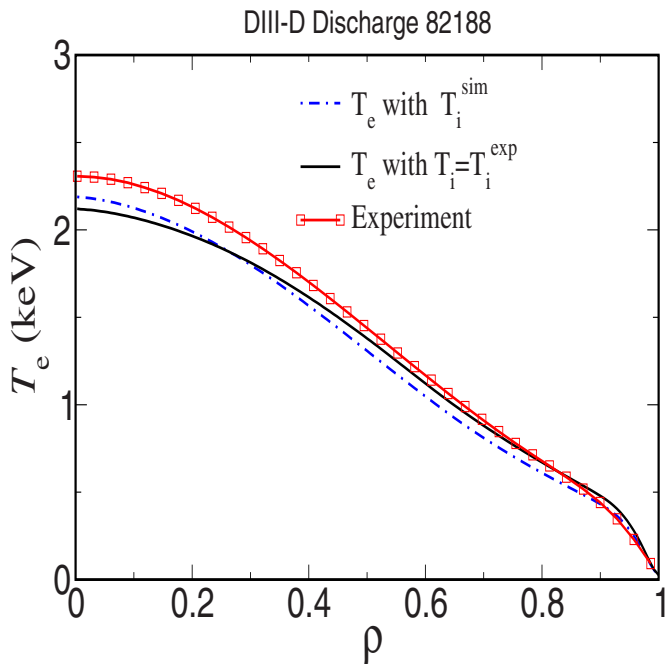
FIG. 10. (Color online) Electron temperature profile from a simulation in which the ion temperature profile is taken from experiment data (solid curve) and a simulation in which both the electron and the ion temperature profiles are evolved simultaneously (dashed-dotted curve).

transport models: (1) Various versions of the GLF23 transport model—the full GLF23 model, the GLF23 model with the trapped electron modes stabilized in the pedestal, and the GLF23 model in which only contributions from the ETG modes are retained; (2) the electromagnetic Horton (WH) model modified by a Jenko threshold for the ETG anomalous transport; and (3) the paleoclassical transport model. These models are implemented in the ASTRA code and applied to predictive modeling of fifteen DIII-D *H*-mode discharges. The simulation results obtained using these models are compared to one another and with experimental data. An integrated modeling protocol is used to simulate only the electron temperature profile while the ion temperature profile is taken from experimental data for each discharge considered. It is found that in the plasma core, where the electrostatic ETG modes are below threshold and, consequently, do not contribute to the GLF23 thermal diffusivity; there is an important contribution to the diffusivity provided by the Horton ETG model in the electromagnetic limit. The paleoclassical transport model together with the ETG component of the GLF23 model are found to be needed in order to produce the observed edge pedestal in these DIII-D simulations. For the 15 discharges considered, the average rms deviation and the average offset for the electron temperature profile are found to be approximately 9% and −4%, respectively, while the average rms deviation and average offset for the electron

temperature pedestal height are found to be about 29% and −11%, respectively.

[1] R. E. Waltz, G. M. Staebler, W. Dorland, G. W. Hammett, M. Kotschenreuther, and J. A. Konings, Phys. Plasmas **4**, 2482 (1997).
[2] W. Horton, P. Zhu, G. T. Hoang, T. Aniel, M. Ottaviani, and X. Garbet, Phys. Plasmas **7**, 1494 (2000).
[3] F. Jenko, W. Dorland, and G. W. Hammett, Phys. Plasmas **8**, 4096 (2001).
[4] J. L. Luxon, Nucl. Fusion **42**, 614 (2002).
[5] W. Horton, B. G. Hong, and W. M. Tang, Phys. Fluids **31**, 2971 (1988).
[6] V. V. Prail and P. N. Yushmanov, JETP Lett. **42**, 278 (1985).
[7] J. D. Callen, Nucl. Fusion **45**, 1120 (2005).
[8] J. D. Callen, Phys. Plasmas **12**, 092512 (2005).
[9] W. A. Houlberg, K. C. Shaing, S. P. Hirshman, and M. C. Zarnstorff, Phys. Plasmas **4**, 3230 (1997).
[10] D. Boucher, J. W. Connor, W. A. Houlberg, M. F. Turner, G. Bracco, A. Chudnovskiy, J. G. Cordey, M. J. Greenwald, G. T. Hoang, G. M. D. Hogeweij, S. M. Kaye, J. E. Kinsey, D. R. Mikkelsen, J. Ongena, D. R. Schissel, H. Shirai, J. Stober, P. M. Stubberfield, R. E. Waltz, and J. Weiland, Nucl. Fusion **40**, 1955 (2000).
[11] W. M. Stacey and R. J. Groebner, Phys. Plasmas **10**, 2412 (2003).
[12] R. J. Groebner, D. R. Baker, K. H. Burrell, T. N. Carlstrom, J. R. Ferron, P. Gohil, L. L. Lao, T. H. Osborne, D. M. Thomas, W. P. West, J. A. Boedo, R. A. Moyer, G. R. McKee, R. D. Deranian, E. J. Doyle, C. L. Rettig, T. L. Rhodes, and J. C. Rost, Nucl. Fusion **41**, 1789 (2001).
[13] D. Schissel, Plasma Phys. Controlled Fusion **38**, 1487 (1996).
[14] C. C. Petty, T. C. Luce, K. H. Burrell, S. C. Chiu, J. S. deGrassie, C. B. Forest, P. Gohil, C. M. Greenfield, R. J. Groebner, R. W. Harvey, R. I. Pinsker, R. Prater, and R. E. Waltz, Phys. Plasmas **2**, 2342 (1995).
[15] C. M. Greenfield, J. C. DeBoo, T. H. Osborne, F. W. Perkins, M. N. Rosenbluth, and D. Boucher, Nucl. Fusion **37**, 1215 (1997).
[16] C. C. Petty, T. C. Luce, J. C. DeBoo, R. E. Waltz, D. R. Baker, and M. R. Wade, Nucl. Fusion **38**, 1183 (1998).
[17] P. B. Snyder, H. R. Wilson, J. R. Ferron, L. L. Lao, A. W. Leonard, T. H. Osborne, and A. D. Turnbull, Phys. Plasmas **9**, 2037 (2002).
[18] ITER Physics Expert Groups on Confinement and Transport and Confinement Modelling and Database, ITER Physics Basis Editorsy, ITER EDA, Naka Joint Work Site, Mukouyama, Naka-machi, Naka-gun, Ibaraki-ken, Japan, Nucl. Fusion **39**, 2175 (1999).
[19] G. Bateman, M. A. Bandrés, T. Onjun, A. H. Kritz, and A. Y. Pankin, Phys. Plasmas **10**, 4358 (2003).
[20] D. Hannum, G. Bateman, J. Kinsey, A. H. Kritz, T. Onjun, and A. Y. Pankin, Phys. Plasmas **8**, 964 (2001).
[21] T. H. Osborne and R. J. Groebner, L. L. Lao, A. W. Leonard, R. Maingi, R. L. Miller, G. D. Porter, D. M. Thomas, and R. E. Waltz, *Proceedings of the 24th European Conference on Controlled Fusion and Plasma Physics*, Berchtesgaden, Germany, 1997 (European Physical Society, Petit-Lancy, Switzerland, 1997), Vol. 21A, p. 1101.
[22] M. Greenwald, R. L. Boivin, F. Bombarda, P. T. Bonoli, C. L. Fiore, D. Garnier, J. A. Goetz, S. N. Golovato, M. A. Graf, R. S. Granetz, S. Horne, A. Hubbard, I. H. Hutchinson, J. H. Irby, B. LaBombard, B. Lipschultz, E. S. Marmar, M. J. May, G. M. McCracken, P. O'Shea, J. E. Rice, J. Schachter, J. A. Snipes, P. C. Stek, Y. Takase, J. L. Terry, Y. Wang, R. Watterson, B. Welch, and S. M. Wolfe, Nucl. Fusion **37**, 793 (1997).
[23] J. E. Kinsey, Nucl. Fusion **39**, 539 (1999).